Laser and Particle Beams (2000), *18*, 109–118. Printed in the USA.

High brightness laser–plasma X-ray source at IFAM: Characterization and applications

S. MARZI,[1] A. GIULIETTI,[1] D. GIULIETTI,[2] L.A. GIZZI,[1] AND A. SALVETTI[1]

[1]Istituto di Fisica Atomica e Molecolare, Area della Ricerca del CNR, Via Alfieri, 1, 56010 Ghezzano, Pisa, Italy
[2]Dipartimento di Fisica, Università di Pisa, and INFM, Via Buonarroti, 2, 56100 Pisa, Italy

(RECEIVED 2 November 1998; ACCEPTED 4 August 1999)

Abstract

A high brightness laser-plasma X-ray source has been set-up and is presently available at IFAM. A wide range of diagnostics has been set up to monitor the properties of the X-ray radiation and to control the main parameters including photon energy, flux intensity, and pulse duration. A beam extractor enables access to the X-ray radiation at atmospheric pressure. A simple, easy-to-use projection microscope has been built which is capable of single-shot micron resolution imaging with digital acquisition. Preliminary biomedical experiments show that the X-ray doses available on a single laser shot exposure of our source fully meet the conditions required for an important class of biological experiments based on X-ray induced DNA damage providing an ideal alternative to the long time exposures needed with X-ray tubes.

1. INTRODUCTION

Laser produced plasmas are now well established as versatile, high brightness sources of X-ray radiation for a wide range of applications in many fields of study including physics, chemistry (Raksi *et al.*, 1995), biology (Kado, 1995), medicine (Barty *et al.*, 1995; Krol *et al.*, 1997) and material science (Mishette, 1997, Allott *et al.*, 1997). One of the great advantages of these sources lies in the possibility of readily customizing the source properties (brightness, pulse duration, spectrum, etc.) as well as the experimental set up required to meet specific user's needs (Gullikson *et al.*, 1992). In this paper we describe the laser plasma X-ray facility presently running at IFAM with particular attention to the physical properties of the source. The preliminary results of recent biomedical applications are also presented and discussed.

2. SCHEMATIC SET UP OF THE SOURCE

The X-ray source is based on a four-stage amplified, pulsed Nd:Yag laser as a plasma producing source. The system is capable of producing single longitudinal mode (SLM) GW pulses at a wavelength of 1.053 μm with either a 3 or 8 ns pulse duration. The pulse is focused with an f/4 optics on the surface of a helically moving cylindrical target at an intensity up to a few times 10^{13} W/cm^2. The helical motion of the target enables a fresh surface of the target to be exposed on each laser pulse with a simple mechanism. A set of basic optical and X-ray diagnostics monitor the focusing conditions in order to ensure a high degree of reproducibility of the interaction conditions from pulse to pulse. A schematic overview of the experimental set up of the X-ray source from the laser beam input to the user end is shown in Figure 1. The laser energy is controlled by varying the charging voltage of the amplifiers and is constantly monitored by a calibrated photodiode. The maximum energy per pulse is 3 J for the 3 ns pulse and 8 J for the 8 ns pulse. The pulse shape is constantly monitored using a photodiode with a response time of $\approx$1 ns. The shape of a typical 3 ns pulse is shown in Figure 2.

A wide range of detectors have been used to characterize the X-ray source spectrally, spatially, and temporally. A miniature, fast P-I-N diode with a subnanosecond temporal resolution is used to monitor the shape of the X-ray pulse (see insert in Figure 2) while a couple of larger diodes are used for X-ray flux measurements. The X-ray pulse duration was typically of the order of the laser pulse duration.

The spectral sensitivity of such P-I-N diodes is shown in Figure 3. The silicon absorption *K*-edge at 1840 eV, clearly visible in the plot, is due to the attenuation of the incident photon flux in the input doped *dead* layer.

2.1. Source characterization: Focal scan

Once the laser pulse is focused on target, the X-ray flux is maximized by adjusting the focusing distance within the

Address correspondence and reprint requests to: Leonida Gizzi, Instituto di Fisica Atomica e Molecolare, Area della Ricerca del CNR, Via Alfieri, 1, 56010 Ghezzano, I.F.A.M., via del Giardino, 7-56127 Pisa, Italy. E-mail: leo@ifam.pi.cnr.it

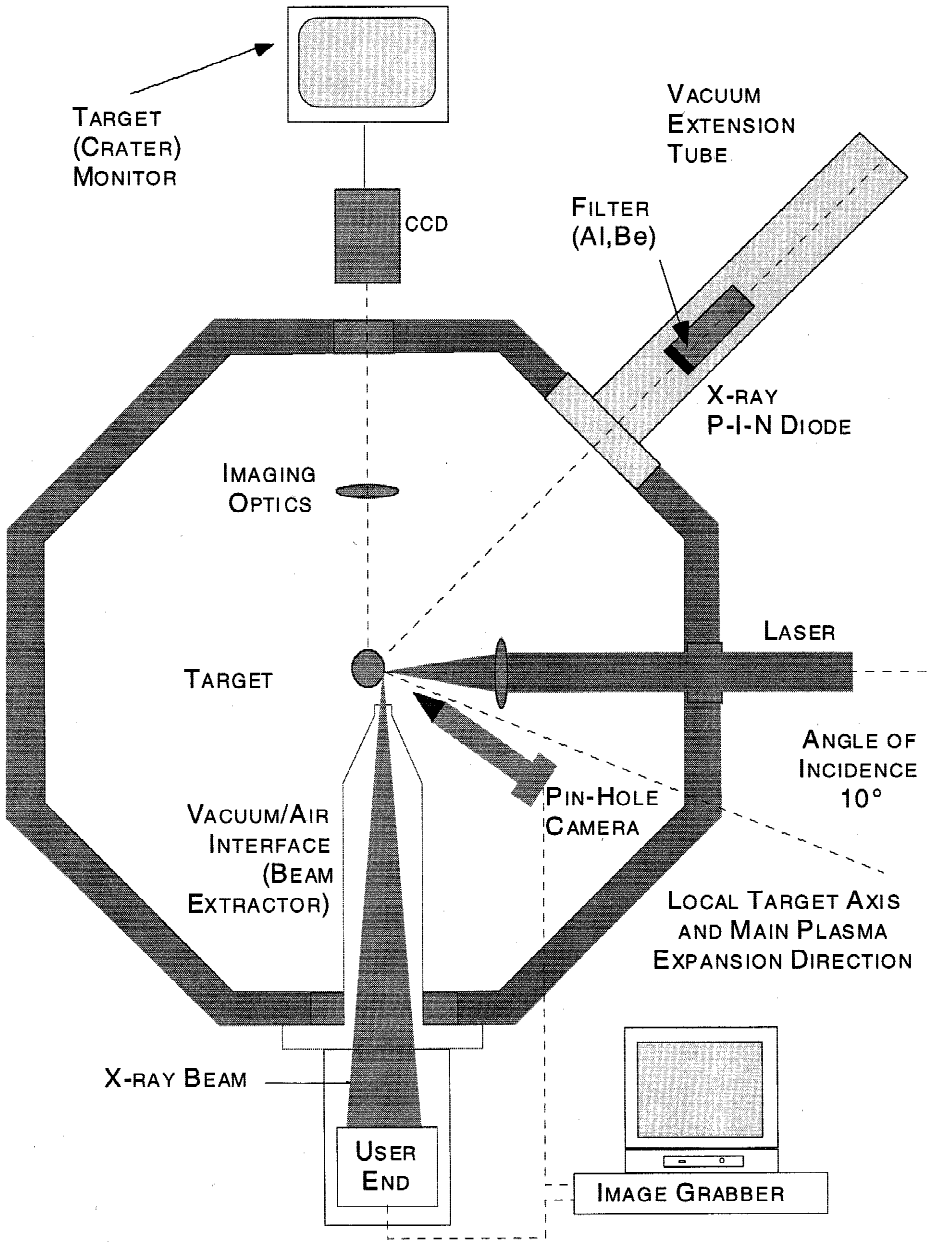

Fig. 1. Schematic view of the experimental set up of the IFAM X-ray source showing the subsystems for the control of the interaction and the main X-ray beam line.

range of a few focal depths of the focusing optics. Figure 4 shows the dependence of the X-ray signal from the P-I-N diode as a function of the distance of the target surface from the beam waist for two different target materials. In the case of the Mo target, the nominal laser intensity was 2×10^{13} W/cm^2 while the diode was 40 cm away from the target and was filtered with a 15-μm thick Be foil. In the case of the Cu target, the nominal laser intensity was 5×10^{12} W/cm^2 and the diode was at 14 cm and was filtered with a 20-μm thick Al foil. Despite the different materials and intensities, in both cases the X-ray emission has a maximum when the target plane is located 2.1 mm beyond the best focusing plane. The same value (within an uncertainty of 100 μm) was also measured for other target materials including Plexiglas, Al, and W. This feature is related to the physics of the interaction and has been interpreted in terms of self-focusing of the incident pulse in the expanding plasma (Biancalana *et al.*, 1993; Giulietti & Gizzi, 1998). Slight differences have been observed in the fall-off of the X-ray signal on both sides of the position of maximum emission as shown in Figure 4 for Mo and Cu.

2.2. Source size

The spatial properties of the X-ray source are monitored by using a CCD pinhole camera with 10 μm spatial resolution

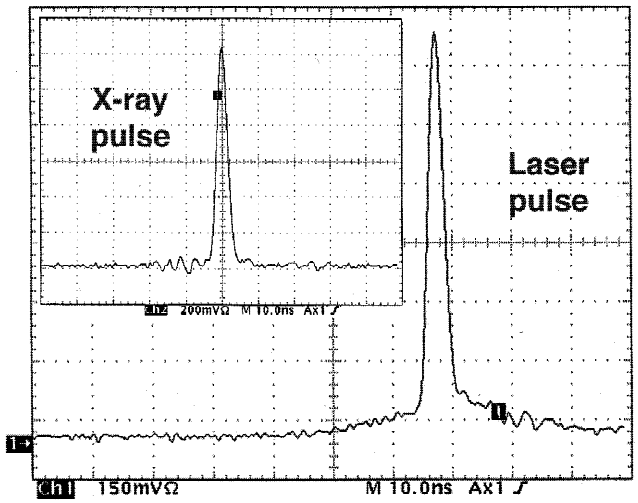

Fig. 2. Shape of the laser pulse with the laser system operating in the 3-ns SLM nominal pulselength regime. The FWHM in this case was 3.1 ns. The shape of the X-ray pulse detected by a sub-nanosecond X-ray P-I-N diode is also shown in the insert.

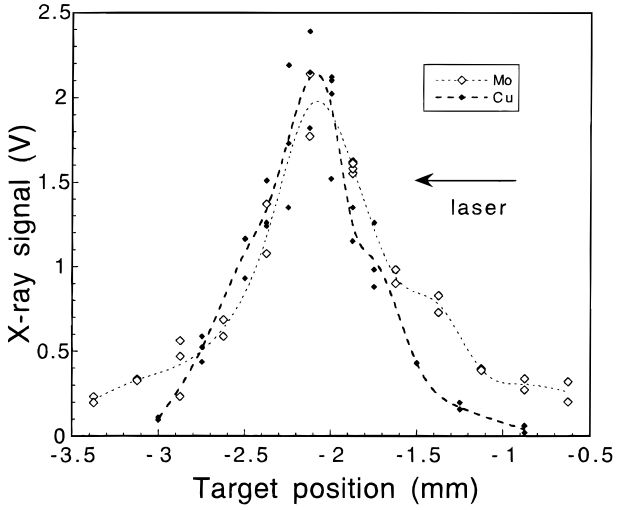

Fig. 4. Focal scan of the X-ray signal for Cu and Mo targets filtered respectively with 20 μm Al and 15 μm Be. The focusing distance was varied by moving the f/4 focusing optics along the optical axis. The X-ray emission is the maximum when the target plane is located 2.1 mm beyond the best focusing plane.

at the object plane. The X-ray image, filtered by a 15-μm thick Be foil, is detected by a windowless CCD camera and stored using an image grabber (see Figure 1). A set of three images obtained from irradiation of a Cu target at three different laser intensities, in the condition of optimum emission, is shown in Figure 5. The images consist of a central bright spot, slightly elongated in the vertical direction, and a weaker tail-like structure. Once the viewing geometry is taken into account, as shown in Figure 6, the width of the central bright structure is found to range between 40 μm (for the lower laser intensity case) and 50 μm (for the higher intensity case). This is very similar to the size of the focal spot (50 μm) measured using alternative techniques (Marzi, 1998). Therefore, the main structure of the source corresponds to the imprint of the laser focal spot. The tail-like structure is due instead to X-ray emission coming from the low-density, hot plasma plume expanding along the local target normal axis at approximately the sound speed $C_s = (\gamma Z k_B T_e/m_i)^{1/2}$, where γ is the adiabatic index, Z is the charge state, T_e is the electron temperature, and m_i is the ion mass. The longitudinal size of the plasma is therefore roughly given by the local sound speed times the laser pulse-length.

From images like those of Figure 5 we can obtain a plasma expansion velocity and, with a simple calculation, an estimate of the temperature of the plasma plume. For a longitudinal plasma extent of approximately100 μm as measured from Figure 5 and a time-scale to reach the steady-state expansion regime of 1 ns we obtain a sound speed of 1×10^7 cm/s. For a Cu target and assuming an ionization degree of $\approx$15, we obtain an electron temperature of $\approx$265 eV.

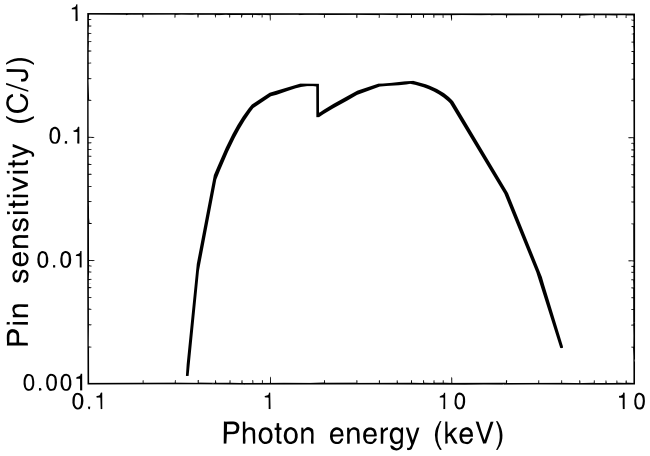

Fig. 3. Typical spectral sensitivity of the X-ray P-I-N diodes used to monitor pulse shape and flux intensity of the X-ray emission.

2.3. Target material and spectral properties

Emissivity and spectral properties of the source can be changed by varying some experimental parameters including target material and laser intensity on target. A systematic study has been carried out to characterize the IFAM X-ray source using five readily available target materials with different atomic numbers, namely Plexiglas ($\langle Z \rangle$ = 3.6), Al (Z = 13), Cu (Z = 29), Mo (Z = 42), and W (Z = 74). The plot of Figure 7 shows the P-I-N diode signal, integrated over the entire spectral window of the detector (with a 15-μm Be filter), as a function of the laser intensity for the five target materials considered. As one can clearly see, Cu targets exhibit a remarkably higher emission intensity compared to the other materials. In particu-

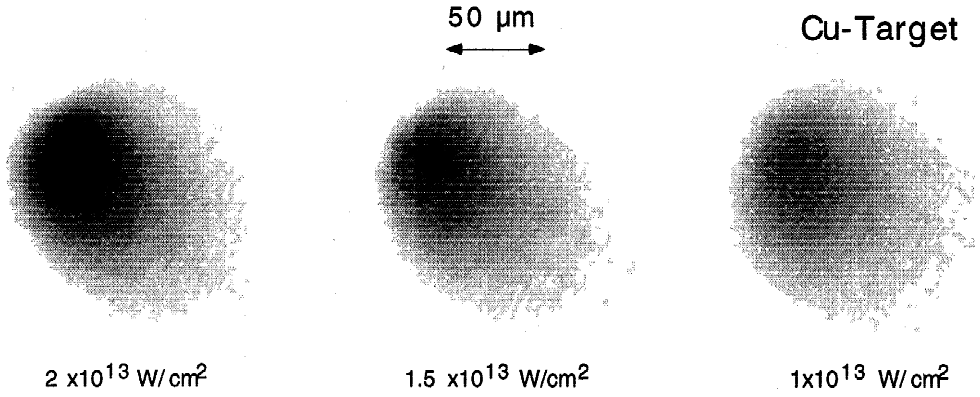

Fig. 5. Images of the X-ray source from a Cu target irradiated at three different laser intensities and obtained by using a CCD pinhole camera.

lar, at the highest laser intensity explored in our study, that is, 2×10^{13} W/cm^2, the signal from Cu targets is 35 times higher than that of Plexiglas and 10 times higher than that of Al. Of great interest for many applications is the spectrum of the emission over a wide range of photon energy. Recently, a new simple technique has been proposed [see Gizzi *et al.* (1996) and references therein] to perform wide-range X-ray spectroscopy using single-photon detection. A very low noise CCD array is used to measure the charge produced by each photon absorbed on a single pixel, provided that the average number of photons per pixel is much less than one. The spectral distribution of the X-ray radiation can be immediately obtained from the charge distribution function, provided that charge diffusion to neighboring pixels is taken into account. This technique, although less accurate than Bragg crystal diffraction, is straightforward from the experimental point of view and is therefore ideal to use as a monitor of the overall performance of the X-ray source. We have implemented this technique on our X-ray source to monitor simultaneously the absolute X-ray flux and the photon energy distribution. Space resolved Bragg diffraction spectroscopy has also been performed for some target materials to investigate the detailed spatial/spectral structure of the source. A systematic description of all these data is beyond the aim of the present work and will be published elsewhere (Gizzi *et al.*, 1999). Also, a large amount of published work exists in this field [see Giulietti and Gizzi (1998) and references therein]. Here, we would

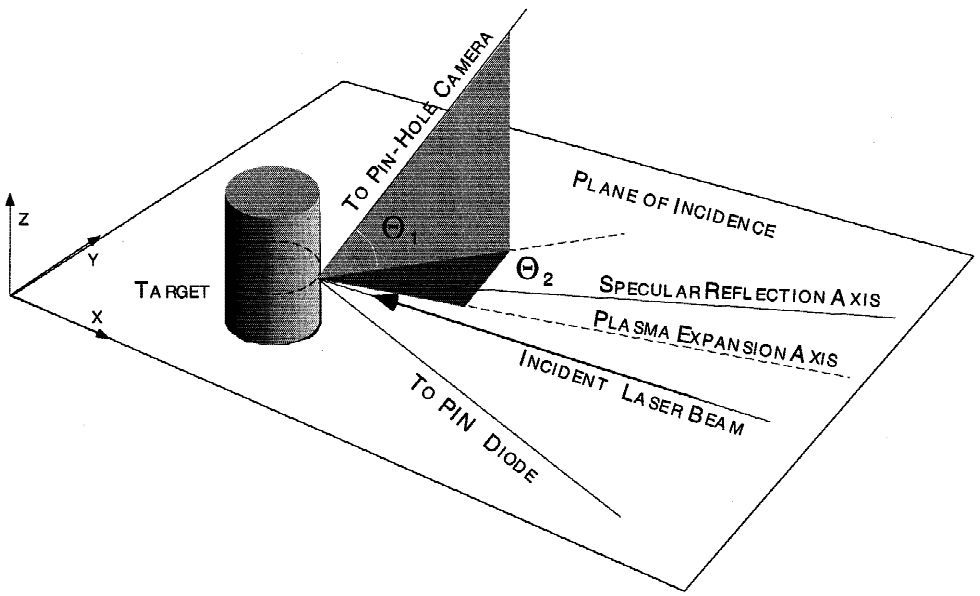

Fig. 6. Geometry of the experimental set up showing the viewing direction of pinhole camera and P-I-N diode with respect to the plane of incidence. In the case of Figure 5, the angles θ_1 and θ_2 were 40° and 20° respectively.

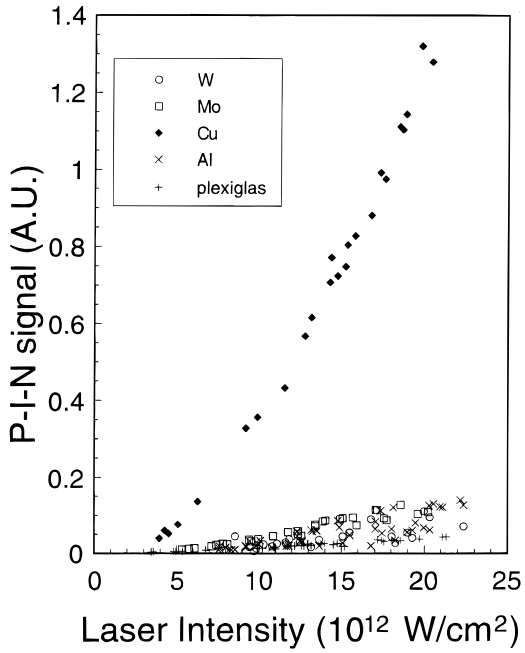

Fig. 7. P-I-N diode signal as a function of laser intensity for 5 different target materials with atomic numbers ranging from 3.6 (Plexiglas) to 74 (W).

like to make some general considerations by simply taking into account the atomic number of the material and the basic physics of radiation emission from plasmas.

2.4. Laser produced plasmas: X-ray spectral properties

Three main processes contribute to the X-ray emission from plasmas, namely bound-bound (lines), free-bound (recombination), and free-free (bremsstrahlung) transitions. Their relative weight is a function of several parameters including the atomic number of the target material and the physical conditions of the plasma (Eidmann & Schwanda, 1991).

In the case of low-Z materials, for example, almost full ionization of the atoms is achieved and, therefore, little bound-bound emission takes place; most of the X-ray emission originates from bremsstrahlung emission. In this case the maximum of the spectral emission for an optically thin plasma is located at a photon energy around $h\nu \approx 2K_BT_e$, that is, for a wavelength $\lambda(\text{Å}) = 6200/T_e(\text{eV})$. For relatively high photon energies the emission intensity decreases exponentially (Kunze, 1987).

In the case of medium-Z materials (e.g., Al), laser plasmas are characterized by highly ionized atoms with a predominance of H-like, He-like configurations (one or two electrons left in the inner K-shell) (Duston *et al.*, 1985). Collisional excitation and radiative de-excitation of these species lead to intense line emission which can be energetically comparable with recombination and bremsstrahlung emission. In this case, the typical emission wavelengths are those of the so-called resonance lines originating from radiative transitions between levels with principal quantum numbers $n = 2$ and $n = 1$ of the H-like and He-like ions. In the case of Al, these wavelengths are 7.17 Å (1729 eV) and 7.75 Å (1600 eV) respectively.

Many other lines are also emitted, however depending on the temperature of the plasma, one or a few of these lines may dominate the spectrum. A typical spectrum of the X-ray line emission from a laser-produced Al plasma is shown in Figure 8. In this case (Macchi *et al.*, 1996) the plasma was generated by a 20 ns Nd laser pulse focused on target at an intensity of 9×10^{12} W/cm^2 and the spectrum was resolved in time using an X-ray streak camera. The dominant species in the plasma was Al^{11+} with the He-α line ($1s^2$–$1s2p$) giving a dominant contribution to the X-ray emission in the keV photon energy range.

A similar spectrum, though centered at higher photon energies, can be obtained using targets with a higher Z-number, provided that the higher temperature required to reach the He-like or H-like configuration can be achieved in the plasma. K-shell radiative transitions in a Si plasma, for example, would provide photons at 1860 eV (He-α line) and 2005 eV (H-α line).

However, as the atomic number increases, one soon reaches the limit in which the plasma temperature required to ionize an atom down to the K-shell cannot be easily achieved in small-scale laboratories. In this case, the dominant X-ray emission comes from L-shell bound-bound transitions. In contrast with K-shell emission, L-shell emission is characterized by a large number of lines mainly from Ne-like and F-like ions (Key, 1988). Due to the high

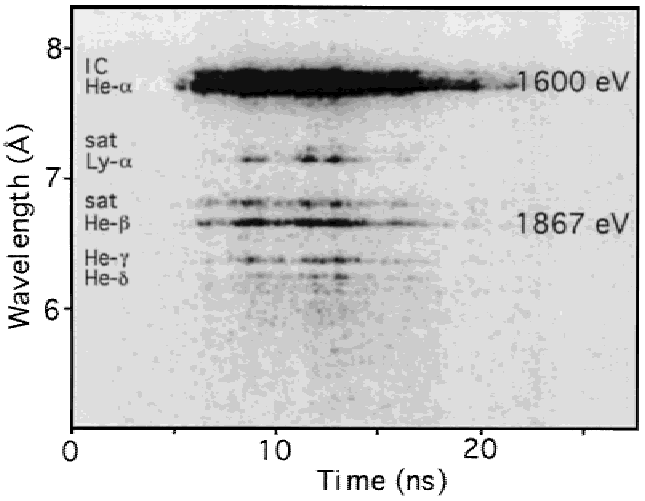

Fig. 8. Time-resolved X-ray spectrum of K-shell emission from an Al plasma produced by laser irradiation with a 20 ns pulse at an intensity of 9×10^{12} W/cm^2 (Macchi *et al.*, 1996).

charge state achieved, such conditions are also particularly favorable for an efficient absorption of laser energy *via* inverse bremsstrahlung. Therefore, the overall conversion efficiency of laser energy into X-rays is particularly high.

In the case of our source, this condition is achieved using Cu targets for which most of the X-ray emission is concentrated in a band of a few hundreds of electronvolts centered at approximately 1 keV. Higher energy photons are still generated due to the bremsstrahlung and the recombination processes, and due to the higher laser energy absorption efficiency, their contribution to the entire X-ray spectrum is higher than in the case of low-Z targets. These circumstances make Cu the most important target material in the interaction regime of our laser-plasma X-ray source.

When using high-Z materials the spectrum consists of a quasi continuum of radiative transitions involving the M, N, and O shells depending on the temperature reached in the plasma (Eidmann & Kishimoto, 1986). In the case of M-shell transitions, the photon energy ranges between 1 keV ($Z \approx 55$) and 3 keV ($Z \approx 80$). In the case of N- and O-shell transitions the typical photon energy is of the order of a few hundreds of eV (Mochizuki & Yamanaka, 1987). Typical target materials used in this case are W, Au, or Bi.

From the discussion given above and from the ensemble of our experimental results we can conclude that Cu, due to its high conversion efficiency, represents the best target material for a general purpose X-ray source in the photon energy range up to ≈5 keV. In specific circumstances, when monochromatic radiation is required, K-shell emission lines from lower Z materials like Al and Si can be used instead. Efficient generation of sub-keV radiation can instead be obtained using high-Z materials like W, Au, Pb, and Bi. All of the data shown below refer to Cu targets unless otherwise specified.

3. A VACUUM-AIR INTERFACE FOR X-RAY BEAM EXTRACTION

As shown in Figure 1, the vacuum chamber which hosts the set-up for the generation of the source plasma has been equipped with a vacuum-air interface which gives direct access to the X-ray beam at atmospheric pressure conditions *via* a 25-μm-thick, 2-mm-diameter, Be window. Such a wall is sufficiently thick to bear the atmospheric pressure while allowing a substantial fraction of the X-ray radiation to be transmitted (Viitanen *et al.*, 1997). This equipment is very useful for soft X-ray irradiation of hydrated *in vivo* biological samples which cannot be placed directly in a vacuum and cannot be enclosed in vacuum-proof containers which would absorb the X-rays, preventing sample irradiation.

In our configuration the sample is placed as close as possible to the Be window in order to minimize the propagation of the X-ray beam in air. In fact, a few centimeters of air are very efficient in absorbing keV photons as shown in the plots of Figure 9. According to these plots, in order to preserve as much as possible of the original spectral properties of the source for photon energies around ≈1 keV, the propagation length in air must be limited to a few cm. Alternatively, fewer and progressively higher energy photons are selected due to absorption in air at increasing distances from the source. A direct observation of the variation of the X-ray flux as a function of the distance from the target has been made using a standard windowless CCD array working in a single photon regime. The CCD detector was placed at sufficiently large distances from the window so that the number of incident photons per pixel was much less than one. In this condition, individual photons can be easily identified on the final image as shown in Figure 10. Images have been taken at progressively larger distances to obtain a direct observation of the X-ray flux, integrated over the entire spectral sensitivity of the CCD array. From the images of Figure 10 we obtain the plot of Figure 11 which gives the photon flux as a function of the distance from the Be window. The data has been fitted taking into account the absorption in air and the $1/r^2$ factor in the assumption that a dominating spectral component exists in the detected spectrum. This analysis gives a dominant photon energy of 2.8 keV which is the result of the combination of the low energy cut off of the Be window (see Figure 9) and the exponential fall-off of the emitted radiation at high photon energy for a plasma of a few hundreds of eV. Extrapolating the X-ray flux for smaller distances (where single photon measurements cannot be made), the photon flux at 10 cm from the source at atmospheric pressure can be estimated to be approximately 3×10^6 ph/cm^2 which corresponds to an X-ray energy flux of 1.5 nJ/cm^2.

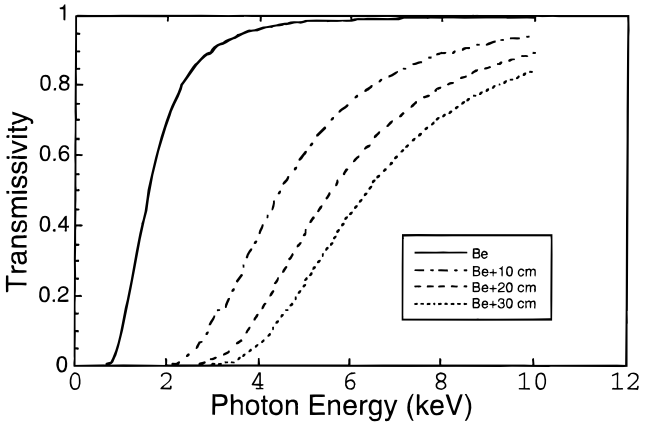

Fig. 9. Transmittivity of the 25-μm Be window used as a vacuum-air interface to extract the X-ray beam. Also shown is the transmittivity for three different thicknesses of air at atmospheric pressure.

4. X-RAY MICRORADIOGRAPHY

In principle, X-ray microscopy is capable of high spatial resolution imaging comparable to that of electron micro-

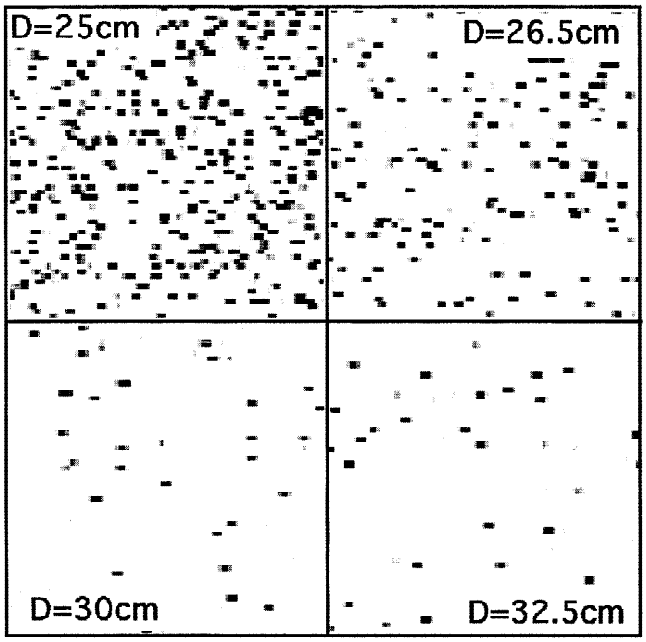

Fig. 10. Single photon measurements of the X-ray flux transmitted through the Be window of the vacuum/air interface taken at four different distances of propagation in air. The images were recorded using a standard, windowless CCD camera as shown in details in Figure 12.

scopes, with the great advantage of a much more penetrating power strongly dependent on the sample atomic number. These properties make X-ray microscopy the ideal technique for high contrast imaging (Aristov & Erko, 1994) of biological samples. The resolution that can be achieved is ultimately determined by the source size which, in the case of laser-plasma X-ray sources is very small, typically of the order of the laser focal spot diameter. This is a very interesting property which, besides the implementation of X-ray optics (Meyer-Ilse *et al.*, 1995), can be readily exploited to obtain, with no need of additional devices, radiography of small, biological samples with a resolution of a few microns and a temporal resolution as high as a few ns. The same equipment used to obtain the data of Figure 10, with small changes, was converted in a projection X-ray microscope as shown in Figure 12.

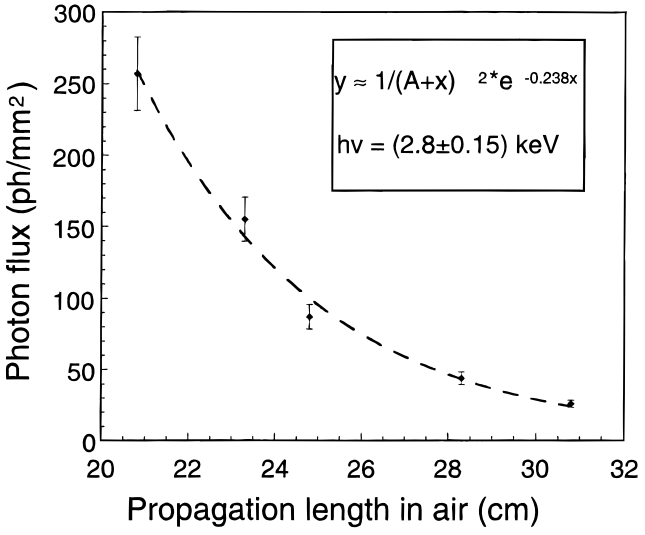

Fig. 11. Flux of X-ray photons as a function of the distance from the vacuum/air interface of the beam extractor. The fitting curve takes into account the absorption in air and the $1/r^2$ factor in the assumption that a dominating spectral component exists in the detected spectrum. This analysis gives a dominant photon energy of 2.8 keV.

This system has been characterized in terms of spatial resolution by using calibrated wires of high-Z material (opaque to X-ray radiation <10 keV). Figure 13 shows the image detected by the CCD using two tungsten wires of 60 μm (left) and 10 μm in diameter. The profile of the 60 μm wire gives a FWHM of 60 μm with a 90%–10% edge width of 21 μm suggesting that the overall resolution of the images is around 20 μm. The image of the 10 μm wire consistently gives a FWHM of 22 μm.

Two factors contribute to the final resolution of the image, namely the transverse size of the source and the spatial resolution of the detector. It can be shown that, due to geometrical considerations, the final resolution, δh is given by:

$$\delta h = \frac{\max\left(\delta_s \frac{q}{p}, \delta_p\right)}{\left(1 + \frac{q}{p}\right)} \tag{1}$$

where p is the object-source distance, q is the object-detector distance, h is the object transverse dimension, δ_S is the source transverse size, and δ_p is the detector spatial resolution due to the pixel size. With the parameters of our set up we find that

$$\delta h \approx \frac{\delta_p}{1 + \frac{q}{p}} \approx \delta_p \tag{2}$$

In other words, the resolution of our imaging system is basically limited by the spatial resolution of the detector. In the case of Figure 13, where a CCD array was used, the resolution is in principle given by the pixel size (8 μm). However, when an X-ray photon is absorbed in the active Si layer of one element of the CCD detector, a large number of electron-hole pairs are generated (typically 1e/3.65 eV). This charge may exceed the well capacity of the single element and may diffuse into neighboring elements resulting in an effective spatial dispersion as shown by the close-up of the single photon images of Figure 10. The final resolution therefore is a function of the incident photon energy and is typically given by 2–3 elements. In our case, this leads to final

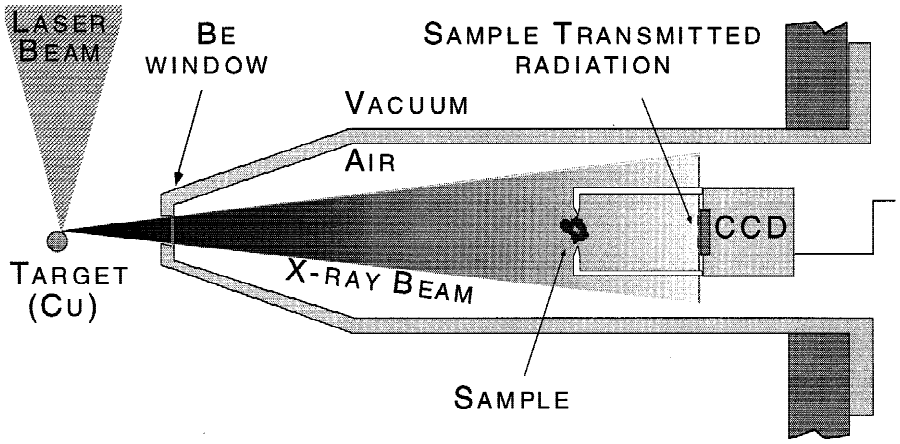

Fig. 12. Set up for X-ray projection microscopy with the IFAM X-ray source. The image is collected by a CCD camera placed behind the sample.

spatial resolution of 20–25 μm which is consistent with the result obtained from the analysis of Figure 13.

It is important to point out that the intrinsic resolution of our system, as due to the source size, is given by $\delta_S q/p$ (penumbral blurring). Therefore, submicron resolution can in principle be obtained in the case of contact microscopy ($q=0$) provided the detector has sufficient spatial resolution. This is the basis of the contact microradiography technique in which the detector consists of a photoresist which usually requires an electron microscope to be "read."

The capabilities of the simple projection microscope to detect complex structures on a microscopic scale have been tested using an ant as an object. The image of Figure 14 shows the structure of the legs with the variety of trans-

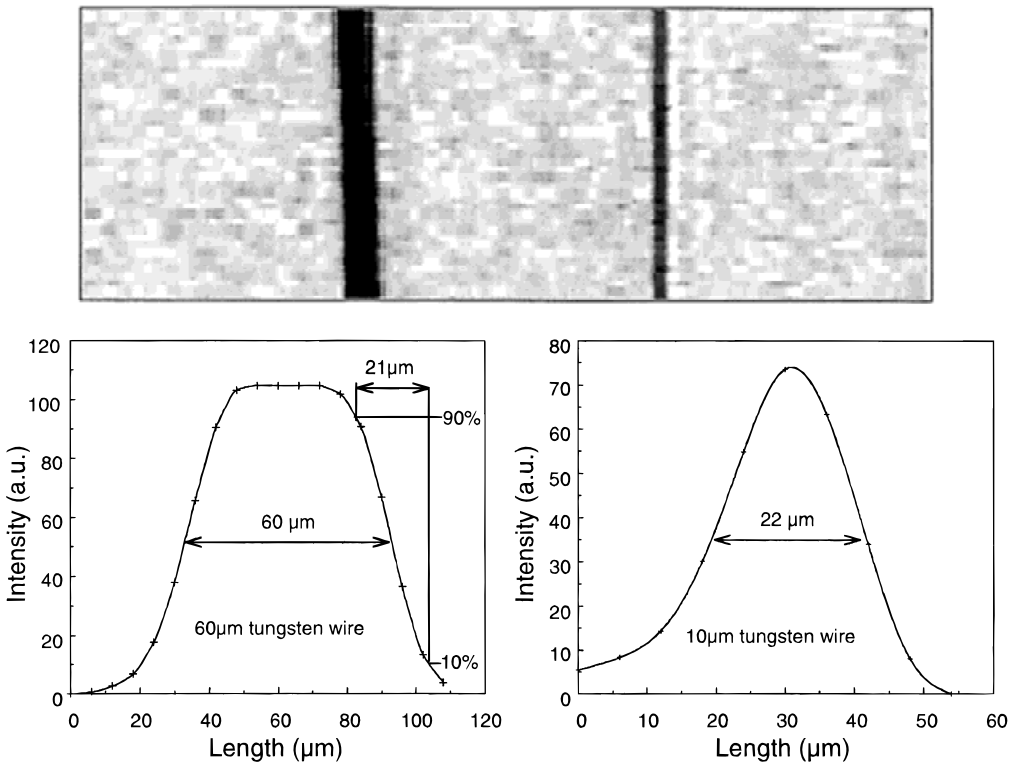

Fig. 13. Projection microscopy of 60 μm (left) and 10 μm (right) W wires for spatial resolution purposes. The profile analysis of the 10 μm wire shows that the spatial resolution is of the order of 10 μm.

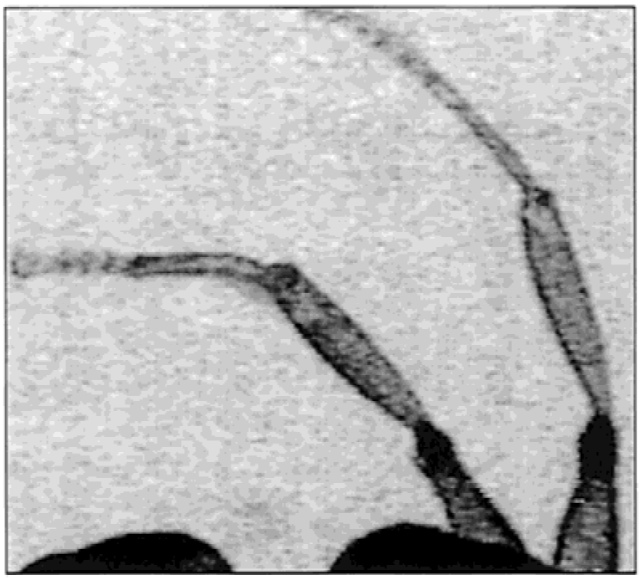

Fig. 14. X-ray projection microradiography of an ant obtained on a single shot exposure using the IFAM source. The image shows the detailed structure of the legs with transparent regions, partially transparent regions and opaque regions.

parent, partially transparent, and opaque structures. It is very important to underline that the image of Figure 14 was obtained with a single laser shot. This gives a direct measure of the source brilliance and of its potential in biological applications.

5. X-RAY INDUCED DNA DAMAGE EXPERIMENTS

Finally, we show the results of a biological experiment (Marzi, 1998) performed with the IFAM source, in collaboration with the Department of Human and Environmental Sciences of the University of Pisa. The experiment was devoted to the investigation of the damage induced on the DNA of human leukocytes by exposure to soft X-ray radiation of known doses and photon energy. Experiments like this are traditionally performed using much higher photon energies (up to one hundred keV) generated by conventional X-ray tubes. Due to the small energy absorption of high energy photons in biological samples and to the limited brightness of X-ray tubes, long (tens of minutes to hours) exposure times are usually required. In these conditions the exposure time may interfere with the repair mechanisms that take place soon after the damage has occurred, making the interpretation of the results more complex. High-brightness laser-plasmas constitute ideal sources of ionizing radiation for these kind of experiments since exposure can be made on a single laser shot. The damage phase can therefore be completely de-coupled from the repair phase. Studies of radiation-induced DNA damage have already been performed in the UV (Melvin *et al.*, 1998) and VUV (Folkard *et al.*, 1998) regions using laser-plasma sources. On the other hand, some specific damage mechanisms (Hutchinson, 1985) become active only at sufficiently high photon energy, thus the need to extend the study to the X-ray region. We have developed an experimental set up which enables the exposure of samples at photon energies of 3 keV at atmospheric pressure. Two samples consisting of a 500-μm-thick layer of agarosio gel containing the sample cells, placed on glass slides, were exposed to 0.5 and 1 mG rays respectively. After exposure, the samples were analyzed using a technique based on single cell gel electrophoresis (SCGE), also known as the *comet* assay (Rydberg & Johanson, 1978). This technique allows a direct evaluation of radiation damage induced on the cell's DNA *via* a measurement of the two most sensitive "comet parameters" for DNA damage, that

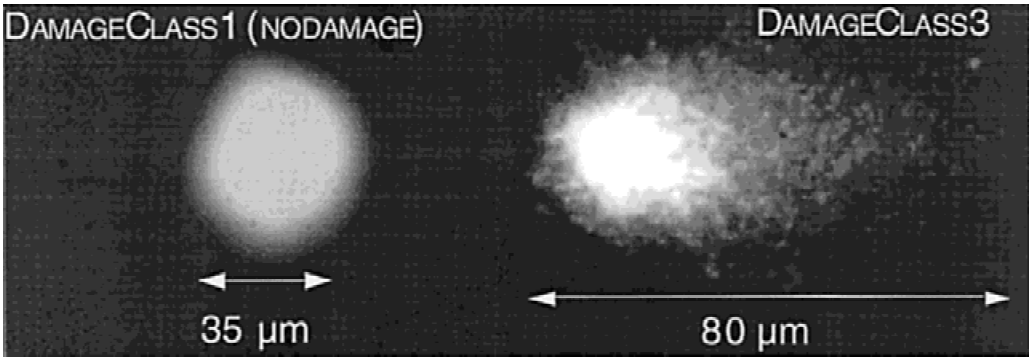

Fig. 15. Left: undamaged (unexposed) cellular nucleus. Right: damaged cellular nucleus after exposure to X-ray radiation. Note the typical cometlike structure with the DNA fragments forming the tail of the comet. The damage is classified according to the length of the tail and to the amount of DNA fragments in it.

is, the inertia and moment of the *tail* formed by the DNA fragments when the cell is placed in an external electric field. Figure 15 shows the image of a damaged cell (right) compared with an undamaged, unexposed one (left). These preliminary results show that our experimental arrangement provides a fast, simple, and controlled way of performing radiation damage experiments. More work is needed to clarify the role of pulsed irradiation with respect to continuous irradiation mode in the repair kinetics of X-ray induced damage.

6. CONCLUSIONS AND FUTURE WORK

The IFAM laser-plasma X-ray source is now fully operational and its potential has already been demonstrated by preliminary bio-medical experiments. A detailed characterization of all the physical properties of the source including target material, laser intensity and duration, focusing conditions, X-ray pulse duration, spatial distribution, and spectral emissivity, has been carried out. All the main source parameters are therefore under control and can be modified according to the user's specific needs. A vacuum-to-air beam extractor, for use of the X-ray radiation at atmospheric pressure has been built and characterized in terms of photon flux and photon energy. Samples can be easily exposed with no need of pretreatment for vacuum-proof conditions.

The system *as is*, is capable of producing projection microscopy with a resolution down to a few micrometers and in a single laser shot. Also, the X-ray doses available on a single laser shot exposure fully meet the conditions required for an important class of biological experiments based on X-ray induced DNA damage, thus providing an ideal alternative to the long exposure times needed with X-ray tubes.

Future work will be concentrated on the progress of the X-ray projection microscope, and in particular on the development of new detection techniques capable of fully exploiting the intrinsic features of the source while preserving the ease of use given by CCD readout systems and the single shot working regime presently available. It is also planned to add suitable X-ray optics to provide the source with tunability and focusing capabilities.

ACKNOWLEDGMENTS

The work presented in this paper was possible thanks to the contribution of many people at IFAM. In particular we would like to thank A. Barbini, V. Biancalana, and A. Lucchesini for many enlightening discussions and original suggestions.

REFERENCES

Allott R.M. *et al.* 1997 In *SPIE Proceedings* **3156**, 138–147.
Aristov V. & Erko A. 1994 (editors), *X-ray Microscopy IV* (Chernogolovka, Russia).
Barty, C.P. *et al.* 1995 In *SPIE Proceedings* **2523**, 286–298.
Biancalana, V. *et al.* 1993 *Europhys. Lett.* **22**, 175.
Duston D. *et al.* 1985 *Phys. Rev. A* **31**, 3220.
Eidmann, K. & Kishimoto, T. 1986 *Appl. Phys. Lett.* **49**, 377.
Eidmann, K. & Schwanda, W. 1991 *Laser Particle Beams* **9**, 551.
Folkard, M. *et al.* 1998 CLF-RAL Annual Report, p. 140.
Giulietti, D. & Gizzi, L.A. 1998 *Rivista del Nuovo Cimento* **21**, 10.
Gizzi, L.A. *et al.* 1996 *Phys. Rev. Lett.* **76**, 2278.
Gizzi, L.A. *et al.* 1999 to be published.
Gullikson, E.M. *et al.* 1992 *X-ray Science and Tech.* **3**, 283.
Hutchinson, F. 1985 *Prog. Nucleic Acid Res. Mol. Biol.* **32**, 115.
Kado, M. 1995 *SPIE Proceedings* **2523**, 194–201.
Key, M.H. 1988 *In Astrophysical and Laboratory Spectroscopy*, SUSSP R. Brown and J. Lang, eds., 388.
Krol, A. *et al.* 1997 In *SPIE Proceedings* **3157**, 156–163.
Kunze, H.J. 1987 In *Astrophysical & Laboratory Spectroscopy*, Proceedings of the 33rd Scottish Universities Summer School in Physics (St. Andrews, Scotland), 187.
Macchi, A. *et al.* 1996 *Nuovo Cimento D* **18**, 727.
Marzi, S. 1998 *Tesi di Laurea*, Dipartimento di Fisica, Università Di Pisa.
Melvin, T. *et al.* 1998 CLF-RAL Annual Report, 136.
Meyer-Ilse, W. *et al.* 1995 *Synchrotron Radiation News* **8**, 29.
Mishette, A.G. 1997 *J. X-ray Science and Tech.* **7**, 98.
Mochizuki, T. & Yamanaka, C. 1987 In *SPIE Proceedings* **733**, 23.
Raksi, F. *et al.* 1995 In *SPIE Proceedings* **2523**, 306–315.
Rydberg, B. & Johanson, K. 1978 *DNA Repair Mechanism.* P. Hanawalt and E. Friedberg, eds. (Academic Press, New York), p. 465.
Viitanen, V.-P. *et al.* 1997 *J. X-ray Science and Tech.* **7**, 130.